Journal of Petroleum Science and Engineering 218 (2022) 110996

Contents lists available at ScienceDirect

Journal of Petroleum Science and Engineering

journal homepage: www.elsevier.com/locate/petrol

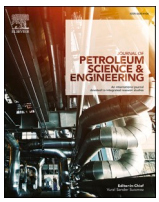

# Pipe flow experiments of unstable oil-water dispersions with three different oil viscosities: Flow pattern, pressure drop and droplet size measurements

Diana Gonzalez [a,*], Heiner Schümann [b], Jørn Kjølaas [b]

[a] Norwegian University of Science and Technology's, S. P. Andersens veg 15a, 7031, Trondheim, Norway
[b] SINTEF Industry, Norway

ARTICLE INFO

*Keywords:*
Oil-water dispersion
Unstable dispersion
Drag-reduction
Flow loop experiments
Droplet size analysis

ABSTRACT

The transport of oil-water dispersions in petroleum production pipelines is difficult to predict and requires special attention since it affects the performance of the entire system. For future field developments it is required to generate accurate predictive models to guarantee an optimal field design. The purpose of this work is to present novel experimental data suitable for improving mechanistic flow models in future works. Oil-water pipe flow experiments were conducted in a stainless-steel flow loop with a L/D ratio of 3766, larger than any comparable setups reported in the literature and sufficient to obtain fully developed flow. A novel level of detail measurements included pressure gradients, density profiles and droplet size distributions.

Three oils with different viscosities (oil A: 1.3 cP; oil B: 7 cP; oil C: 22 cP) and brine (3.5 wt% NaCl) as the water phase constituted the three fluid systems used. For each fluid system, several flow rates, and a wide range of water fractions were studied. The fluids were not stabilized by any type of chemical additives.

The oil viscosity influences the dispersion behavior, especially for oil continuous flow. For higher oil viscosities the dispersion tends to be more homogeneous, and the pressure drop increases due to increasing wall friction. The droplet size decreases as the oil viscosity increases, presumably due to higher shear stress. Water continuous flows, on the other hand, are less affected by the oil viscosity. A strong drag reduction was found for dispersed flow of all three oils and both oil and water continuous flow. A simple model for the dispersion viscosity and drag reduction was developed based on additional bench scale characterization experiments. With this model the pressure drop could be predicted with good agreement.

The data reported in this paper will facilitate the development and validation of mechanistic models for predicting oil-water flows. Previous modelling efforts have been hampered by a lack of detailed measurements, in particular droplet size measurements, hence we believe that this data will allow for significant advancements on the modelling side.

## 1. Introduction

The Norwegian multiphase flow technology cluster have had a huge success in enabling multiphase hydrocarbon transport from wells to processing facilities (Strømsheim and Haugnes, 2012). Without the cost savings of this technology, many NCS (Norwegian continental shelf) fields would not have been possible to develop. In fact, most future developments on the NCS will be realized through tie-back solutions where accurate multiphase flow predictions are a requirement for successful subsea developments (OG21 group, 2021). The credibility of the simulators is so high that new developments have repeatedly surpassed former solutions with respect to transport length and complexity. The record for gas dominated multiphase transport is currently 149.7 km. However, the reach for liquid dominated transport is much less (69.8 km) (Barton et al., 2019). One important reason for this difference is the challenging interaction between fluid dynamics and interfacial chemistry of liquid dominated flows that make the prediction of the hydrodynamic behavior very difficult.

Both experimental evidence (Valle, 1998; Elseth, 2001; Angeli, 1996; Nädler and Mewes, 1997) and modelling (Elseth, 2001; Valle, 2000; Brauner, 2003; Picchi et al., 2015; Rodriguez and Oliemans, 2006) show that the existence of dispersed phases affects the pressure loss in multiphase flow significantly. This is caused by changing the present flow pattern and by the high effective viscosities of the dispersions itself

* Corresponding author.
*E-mail address:* diana.rengifo@ntnu.no (D. Gonzalez).

https://doi.org/10.1016/j.petrol.2022.110996
Received 4 January 2022; Received in revised form 26 July 2022; Accepted 18 August 2022
Available online 7 September 2022

(Pal and Rhodes, 1989). Still, effective dispersion viscosities and other phenomena, crucially influencing the pressure drop in a pipe, are highly dependent on the fluid system and cannot be explained by means of physical fluid properties only, as demonstrated by (Valle, 2000). Repeating flow loop experiments with different model and crude oils resulted in very different flow behavior, and dispersion formation could lead to either increasing or decreasing pressure drop. As found by (Pal, 1993), in addition to a viscosity effect, a drag reduction mechanism can also be present in unstable dispersions leading to the opposite effect on the pressure drop. Drag reduction was also observed by several other authors (Angeli and Hewitt, 1998; Kumara et al., 2009; Soleimani, 1999). While drag reduction was suspected to be caused by the presence of dynamic coalescence and break-up processes, the exact mechanism was not fully understood. In a modelling approach by (Ngan, 2011) both effects were treated separately as an effective viscosity and an empirical correlation for the effective friction factor, where the drag reduction was proportional to the dispersed phase fraction. Based on his earlier findings (Pal, 2007), proposed a new effective viscosity model combining both effects, where the effective viscosity is expressed as a function of dispersed-to-continuous phase viscosity ratio, capillary number, and dispersed volume fraction. However, he also mentioned the importance of droplet size governing the ability of droplet deformation in turbulent flow and finally leading to a turbulence dampening effect. The influence of droplet size distributions was earlier demonstrated in (Pal, 1996). In a later work (Omer and Pal, 2013) mentioned that the drag reduction behavior of unstable dispersions is explained in terms of the droplet size being much larger than the turbulent length scale and, hence suppressing turbulence. In the presence of surfactants, the droplet size is reduced falling below the turbulent length scale.

Drag reduction was also demonstrated by (Rodriguez et al., 2012) where a thin laminar water film near the wall around the dispersion core formed effectively reducing the friction factor. A core-annular flow model was proposed for the investigated type of flow.

Turbulent drag reduction is also well-known in the presence of low concentrations of flexible polymers (viscoelastic polymer solutions) (Pinho et al., 2008), also known as the Toms phenomenon. Even if much different in size, shape, and concentration there might be some analogy when compared with droplet dispersions.

As evidenced by the literature survey summary above, oil-water flows have been investigated experimentally thoroughly by many authors over the last 30 years. It is however our view that previous experimental works have all had certain limitations that impede progress on the modelling side. Indeed, to derive and validate a mechanistic model for oil-water flow, detailed cross-sectional information is needed, and this is lacking in most of the previous works. Another shortcoming of previous campaigns is that the droplet size distributions have not been measured. The droplet size is a crucial parameter in any model accounting for droplet dispersion because the gravitational drift of droplets is critically dependent on this. Another matter of concern in some of the previous campaigns is whether the flow was fully developed. Because the gravitational drift of droplets in oil/water systems is typically quite slow (due to the small density difference), entrance effects can be a problem for oil-water flow experiments. Specifically, if the pipe test section is not long enough, there is a risk that the flow at the point of measurement is partially a product of the oil/water mixing point, and that the flow is not fully developed. In the present experiments we have used a very long test section (212 m, or 3766 pipe diameters) to avert this problem. Finally, in the experimental works on oil-water flow reported in the literature, we have not found any systematic studies of the effect of the oil viscosity. In petroleum transport systems, the oil viscosity will typically vary significantly because of temperature variations, hence this seems to be an important deficiency that we cover in the present work.

In this work, new oil-water pipe flow experiments are presented for three different oil viscosities, performed in an extensive scientific flow loop with advanced instrumentation. Experiments were performed for several flow velocities covering the transition from separated to dispersed flow and the complete range of water fractions. Fluids were not stabilized by any type of chemical additives, which will be subject to future work. It was therefore not the intention to mimic a specific crude oil behavior but rather studying a system of well characterized fluids. Unknowns introduced by the complex fluid chemistry of crude oils was therefore avoided. Also, the covered range of oil viscosities (1.3 cP to 22 cP) is restricted when comparing with the wide range of relevant crude oil viscosities. The focus of the work was on a detailed in-situ characterization of phase distributions and droplet characteristics of the flow as basis for explaining the resulting pressure drop measurements. Finally, data should be used for model improvements.

The work presented is the first of a series of activities performed to advance the understanding of oil-water flow in transport pipelines, with focus on dispersed flow patterns and droplet behavior. These activities are part of a knowledge-building project for the industry called NEXFLOW – Next generation oil-water flow models in production technologies. NEXFLOW is a collaboration between the Norwegian partners SINTEF, NTNU, TotalEnergies EP Norge, and the Brazilian partners ISDB Flowtech and PUC Rio.

## 2. Experimental setup

The experiments were performed in the so-called medium scale flow loop at SINTEF's multiphase flow laboratory at Tiller, Norway. In the closed flow loop the fluids were separated completely in an 11 $m^3$ separator after passing the test section. A centrifugal oil and water pump were used to recirculate the fluids. The fluids were merged in a Y-type manifold at the test section inlet. The test section itself consisted of a stainless-steel pipe with inner diameter of ID = 56.3 mm and total length of L = 212 m, whereof four straight sections of 48 m length were connected with 180° bends with 1 m bend radius. The test section had an angle of 0.1° from horizontal alignment such that the second loop could be placed on top of the first one. With a length-to-diameter ratio of more than 3700, the flow loop had one of the longest reported test sections. This was important to reach fully developed conditions. Development lengths can be extensive for oil-water flow and any inlet configuration will lead to disturbance of the flow. (Karabelas, 1978) mentioned a L/d > 600 as a minimum required for reaching a steady state for oil-water flows which were not intentionally disturbed at the inlet. A sketch of the test section with main instrumentation is shown in Fig. 1. In total, eight side mounted pressure transducers were used for measuring the pressure development along the pipe. Five vertically traversable gamma beam densitometers were used to non-intrusively measure cross sectional density profiles of the test section. A more detailed description of the gamma densitometers can be found in (Kjølaas and Wolden, 2021). Two transparent sections were used for video monitoring. Three sample points were connected to a CANTY InFlow Particle Sizer for droplet characterization. The sample probe was traversable in height. Finally, a wall film sensor was used for measuring the local wetting of the pipe wall. The sensor consisted of eight electrodes with circular placement in the pipe. The electrodes were flash mounted with the pipe wall and measured the conductivity of the contacting fluids. Instrument positions are summarized in Table 1.

## 3. Fluid systems

### 3.1. Fluid properties

As oil phase three blends of the white oils Exxsol D60 and Primol 352 were used to obtain different viscosities. The water phase consisted of tap water with 3.5 wt% sodium chloride. No temperature control was installed leading to a variation of the operating temperatures between 23 and 30 °C during the campaign. The system was evacuated, flushed with nitrogen and sealed with a little overpressure of 0.5 bar in order to remove most oxygen and prevent fouling during the campaign. Analyses

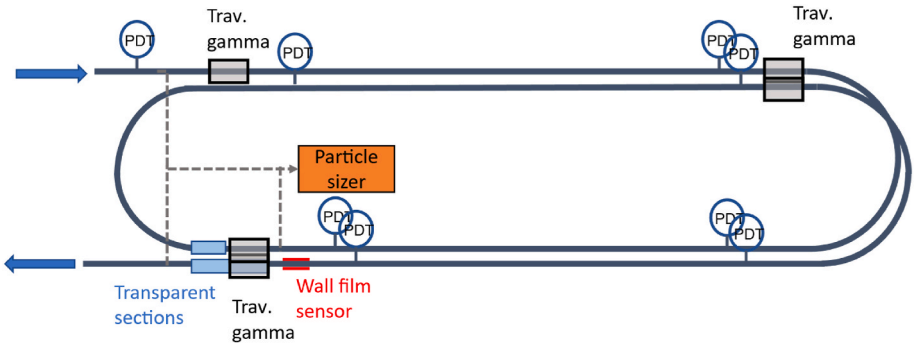


**Fig. 1.** Sketch of the test section and placement of instrumentation (Distances not to scale and instrument placements are just indications.).

**Table 1**
Instrument positions.

| Instrumentation | Position [m] |
|---|---|
| Inlet choke valve **with ΔP measurement** | 0 |
| **Pressure transducers** | 0.08, 49.34, 56.76, 100.26, 108.20, 153.40, 160.80, 204.31 |
| **Transparent sections** | 103–103.5, 206.5–207.5 |
| **Traversing gamma densitometers** | 1.67, 50.34, 102.65, 154.40, 206.70 |
| **Droplet sampling probes** | 2.43, 100.57, 209.50 |
| **Wall film sensor** | 206.40 |

of samples taken before and after the campaign showed no difference in the physical properties. Fluid properties from laboratory measurements are summarized in Table 2.

### 3.2. Rheology measurements

Rheometers are typically used for measuring single fluid viscosities under controlled conditions. However, for measuring dispersion viscosities a rheometer will have limitations. Obstacles are unrealistic geometry of a rheometer or inhomogeneous distribution of the droplets or even separation due to for example centrifugal forces as present in rotary rheometers. In the presented work a mini-loop was used as pipe viscometer for additional characterization of dispersions produced with oil A. The working principle is comparable to the main flow loop as described in section 2 but of considerably smaller scale. A 600 L tank is used as fluid storage and settling separator. From there, oil and water are pumped separately with controlled rates to a mixing section. The dispersions are produced in a mixing valve with controlled pressure drop. The flow enters a 2 m long, 8 mm inner diameter vertical steel pipe. The measured pressure drop over this test section is used to calculate the friction factor, $f$, and further viscosity, $\mu$, of the flowing dispersions, see Fig. 2 for a principle sketch. Due to limitation in the pump capacity, which was not able to deliver high viscosity fluids at sufficiently high rate, the same experiment could not be repeated with oil B and C.

The following procedure was used: First, for a fixed water cut (WC), defined as the inlet water fraction ($WC = Q_{water}/(Q_{water} + Q_{oil})$, a range of laminar points with Reynolds numbers, $Re$, smaller than 2000 were

**Table 2**
Fluid properties.

| Oil | Viscosity @ 25 °C [cP] | Density @ 27 °C [kg/m3] | IFT* – initial value @ 22 °C [mN/m] | IFT* – after 10 min @ 22 °C [mN/m] |
|---|---|---|---|---|
| A | 1.3 | 777 | 53.4 | 42.0 |
| B | 6.8 | 817 | 61.2 | 48.2 |
| C | 20.5 | 833 | 64.7 | 56.0 |

*** IFT: interfacial tension between oil and water**

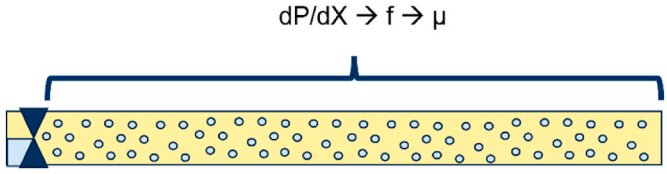


**Fig. 2.** Principle of the mini-flowloop used as pipe viscometer.

tested to obtain the dispersion viscosity. For laminar flow the viscosity, $\mu$, can be back calculated from the pressure drop, $dP/dx$, by equations (1)–(3).

$$f = \frac{dP}{dx}\frac{D}{2}\frac{1}{\rho U^2} \tag{1}$$

$$Re = \frac{f}{16} \tag{2}$$

$$\mu = \frac{\rho U D}{Re} \tag{3}$$

Here $D$ is the pipe diameter, $\rho$ is the mixture density, U is the mixture velocity of the flow and $f$ is the Fanning friction factor. Equations (1)–(3) are valid for single phase flow. We assumed a well-mixed dispersion throughout the test section which was guaranteed by the vertical pipe orientation and a rather high pressure drop over the mixing valve of 1 bar. With this assumption, the mixture is treated as a single fluid with a mixture density, making valid the use of equations (1)–(4).

In the second step, points with higher Reynolds numbers, $Re > 2000$ (turbulent flow and transition to turbulent flow), were tested. The friction factor calculated from the pressure drop measurements for the clearly turbulent flow ($Re > 4000$) were compared with the theoretical friction factor. For the theoretical friction factor a dispersion viscosity was used as obtained from the laminar flow measurements. The Blasius equation for smooth pipes, eq. (4) showed to be well suitable for the hydraulic pipe used as test section and was applied for calculating the friction factor in the turbulent regime. The friction factors from the measurements were still obtained using eq. (1).

$$f = \frac{0.0791}{Re^{0.25}} \tag{4}$$

Examples of characterization experiments are shown in Fig. 3 for different water cuts. For single phase experiments (pure oil 0% WC, pure water 100% WC) the measurements (circles) agree well with the theoretical friction factor (lines). For dispersions the measured friction factors in the turbulent regime were considerably smaller than the theoretical ones. Similar results were found by (Pal, 1993) with a comparable method when testing unstable dispersions of refined mineral oil and tap water. Pal attributed this drag reduction behavior to turbulence modification in the presence of a dynamic coalescence/-breakup process. However, the detailed mechanism is unclear.

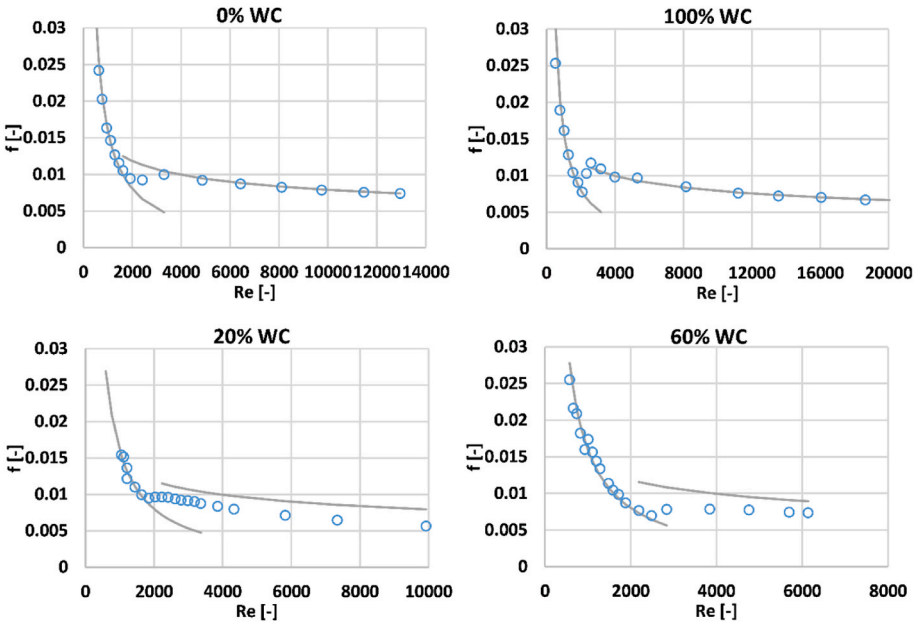


**Fig. 3.** Measured friction factors for different water cuts for oil A. Circles are measurements. Lines are the theoretical friction factors for laminar flow, eq. (2) and turbulent flow, eq. (4).

The measured dispersion viscosities from the laminar flow experiments are summarized in Fig. 4. Relative viscosities are plotted as function of the dispersed phase fraction. Results were divided into oil continuous and water continuous systems. In both cases the measurements are in good agreement with an empirical expression for the relative viscosity of oil-water systems proposed by (Pal and Rhodes, 1989), eq. (5).

$$\mu_{rel-P\&R} = \left(1 - 0.8415\frac{\varphi}{\varphi_{100}}\right)^{-2.5} \tag{5}$$

Here, $\varphi$ is the dispersed phase fraction and $\varphi_{100}$ is the dispersed phase fraction which would give 100 times the single-phase viscosity. A value of $\varphi_{100} = 0.765$ was used.

From the experiments in the turbulent flow regime the relative friction factor was estimated by comparison with the theoretical one calculated as described above. The relative friction factor illustrates the drag reduction effect in the system. According to (Pal, 1993), drag reduction is a phenomenon that only takes place in turbulent flow, while the dispersion viscosity effect affects the pressure drop in both laminar and turbulent flow. Thus, by conducting experiments in both laminar and turbulent flows, we can separate the effects of dispersion viscosity and drag reduction. Specifically, we measure the emulsion viscosity effect in laminar flow, and we measure the sum of both effects in turbulent flow. By assuming that the same dispersion viscosity law applies in laminar and turbulent flow, we can isolate the drag reduction effect. The results are shown in Fig. 5. The drag reduction behavior increases with the dispersed phase fraction. However, oil continuous points show a much stronger drag reduction. Using a simple linear expression (shown as dotted lines in Fig. 5) the relative friction factor for turbulent flow of oil A can be expressed as:

$$f_{rel} = 1 - \eta\varphi \quad with \quad \eta_{oil} = 1.18; \quad \eta_{water} = 0.5 \tag{6}$$

## 4. Test matrix

The test matrix including points for all three fluid systems is shown in Fig. 6. Here the WC is defined as the inlet water fraction. Note that the local water fraction can differ from the WC. $U_M$ is the mixture velocity. For each fluid system, a combination of different $U_M$ and WCs was tested. This allows to study the transition from separated to dispersed flow. The WCs cover the range from 0% to 100%, allowing us to study both oil-in-water and water-in-oil dispersions, as well as the inversion point of the flow. The maximum mixture velocity was limited by the pump performance and reached 4 m/s for oil A and 3 m/s for oil B and C.

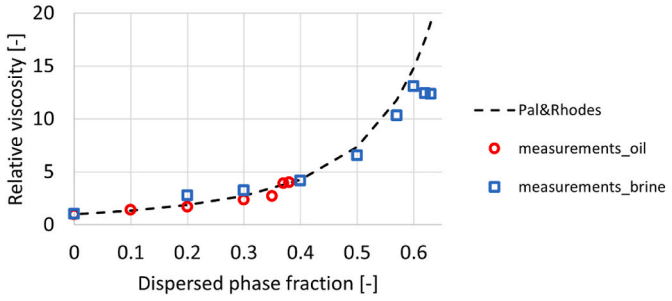


**Fig. 4.** Measurements of dispersion viscosities for oil A as obtained in the pipe viscometer. Measurements are compared with the Pal & Rhodes equation. Red circles are oil continuous points, blue squares are water continuous points. (For interpretation of the references to color in this figure legend, the reader is referred to the Web version of this article.)

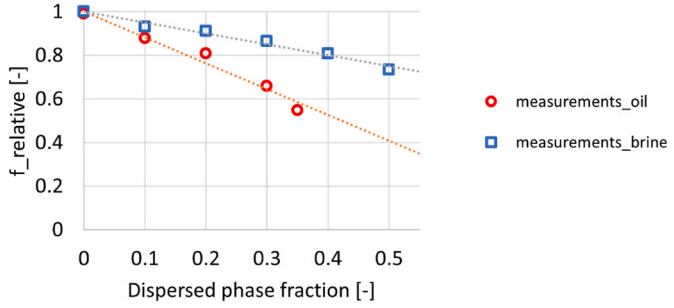


**Fig. 5.** The relative friction factor for oil A obtained from comparing measurements in the turbulent flow regime with the theoretical friction factor. Red circles are oil continuous points, blue squares are water continuous points. (For interpretation of the references to color in this figure legend, the reader is referred to the Web version of this article.)

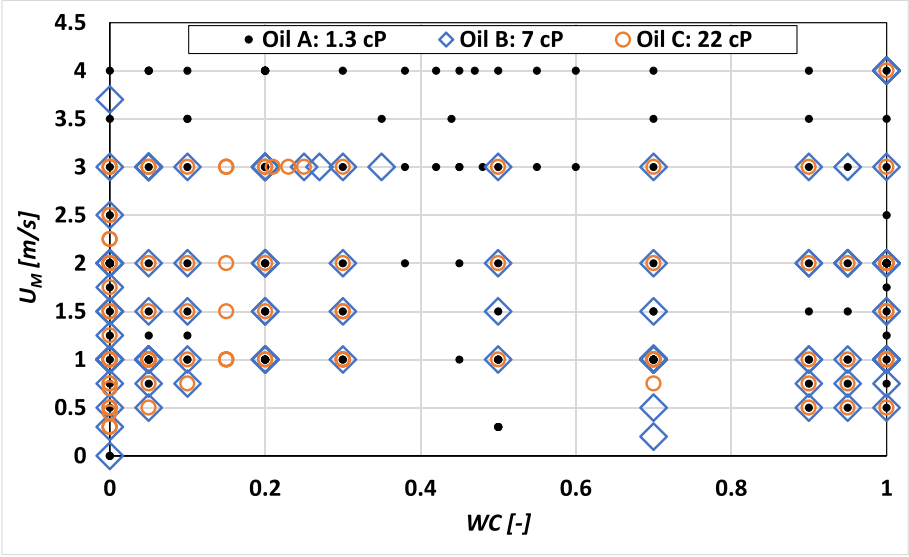


**Fig. 6.** The test matrix shows the combinations of velocity and WC used for the experiments for each fluid system.

This was sufficient for reaching a full transition to dispersed flow.

## 5. Results

### 5.1. Flow regimes

The local water fractions were measured using five vertically traversable gamma beam densitometers. The data collected allowed identifying the different flow regimes that were present during the experimental campaign. When uncertain, additional measurements from the pipe wall film sensor were used. These measurements are based on pointwise conductance measurements in the pipe perimeter giving a distinctive high signal for water continuous flow, low signal for oil continuous flow and noisy signal when dispersions were present. For the full set of experimental points tested, the following flow regimes were observed:

**Separated flow**: In this flow regime the two fluids are separated in different continuous layers located at the top and the bottom of the pipe according to their respective density. At low velocities, up to 1 m/s, fully separated flow is observed. As the velocity increases, the phases start to mix and a layer of drops appears at the interphases between the two phases, this regime exist between 1 and 1.5 m/s.

**Dispersed flow**: Here one fluid is dispersed in the form of droplets into the other phase, which is continuous. Two categories of dispersed flow regime were observed: heterogeneous dispersed flow and homogeneous dispersed flow. Dispersed flow can be either oil or water continuous.

The heterogeneous dispersion exists when the drops gather close to the top or the bottom of the pipe and, in some cases, even a clear layer of the pure continuous phases is observed. The criteria chosen by the authors to consider a dispersion as heterogeneous is that the difference between the water fraction at the top and the bottom of the pipe is higher than 0.2. This flow pattern was observed at low and intermediate $U_M$. At $U_M$ lower than 1.5 m/s, the heterogeneous dispersion, with a clear layer of the continuous phase, was observed for extreme values of water fraction (low and high). At higher velocities, between 2 and 3 m/s, the heterogeneous dispersion, without clear layer of the dispersed phase, appears at intermediate water fractions.

As stated above, we defined the flow to be homogeneous when the difference between the water fraction at the top and bottom of the pipe is 0.2 or less. Here, no clear layer of the continuous phase is observed, and the dispersed droplets are uniformly distributed in the pipe. This flow pattern appears at intermediate and high velocities. For intermediate velocities, 2 m/s, the homogeneous dispersions appear at low and high water fractions only. At high velocities (3 m/s and higher), the mixture is homogeneously dispersed for all water fractions. Maps of the flow patterns observed for the different combinations of mixture velocity and water fraction are presented in Fig. 7.

Figs. 8–10 show the local water fraction ($\alpha_W$) for the three oils studied and $U_M$ of 1, 2 and 3 m/s. In general, and at low mixture velocities, we observed similar flow regimes for the different oil tested. As the velocity increases, the dispersed flow regime tends to be more homogeneous for higher oil viscosity.

### 5.2. Pressure drop

Fig. 11 to Fig. 13 show the pressure drop for the three fluid systems used, where the mixture velocity, $U_M$, was varied between 0.5 m/s and 4 m/s, and the inlet water fraction from 0 to 1. The pressure drop increases with the mixture velocity due to the effect of increasing wall shear stress.

For the oil A (1.3 cP), in Fig. 11, at mixture velocities of 1.5 m/s and lower, the flow regimes observed were separated flow and heterogeneous dispersed flow. At 2 m/s, the flow regimes observed where heterogeneous and homogenous dispersed flow, and some drag reduction is observed for the lower and higher values of water fraction (most homogenous flow).

At $U_M = 3$ m/s to 4 m/s, the flow in the pipe is always homogenously dispersed. The pressure gradient increases toward a peak at the phase inversion region due to the increase in effective viscosity. For the case of $U_M = 3.5$ m/s, the peak is not observed, but this can be attributed to the lack of data points in the phase inversion region. Drag reduction is observed for the three highest velocities (3, 3.5 and 4 m/s), for both oil continuous and water continuous dispersions.

Fig. 12 and Fig. 13 show the pressure drop for oil B (7 cP) and oil C (22 cP) respectively. Same as for oil A, the flow regime is separated flow and heterogeneous disperse flow at $U_M = 1.5$ m/s and lower, while for higher $U_M$ the flow regime becomes heterogeneously or homogeneously dispersed. For higher $U_M$, no distinct peak at the phase inversion was observed anymore for oil B and C. However, at this velocity, the phase inversion region can be identified as an abrupt reduction in the pressure drop. Phase inversion depends on the viscosity ratio and moves towards lower WCs for increasing oil viscosity. Here, the pressure drop is largely governed by which phase is in contact with the pipe wall. For oil continuous flow (with high oil viscosity), the wall friction is large, yielding large pressure drops, while for water continuous flow, the opposite is true. The inversion WCs for oil A, B and C were

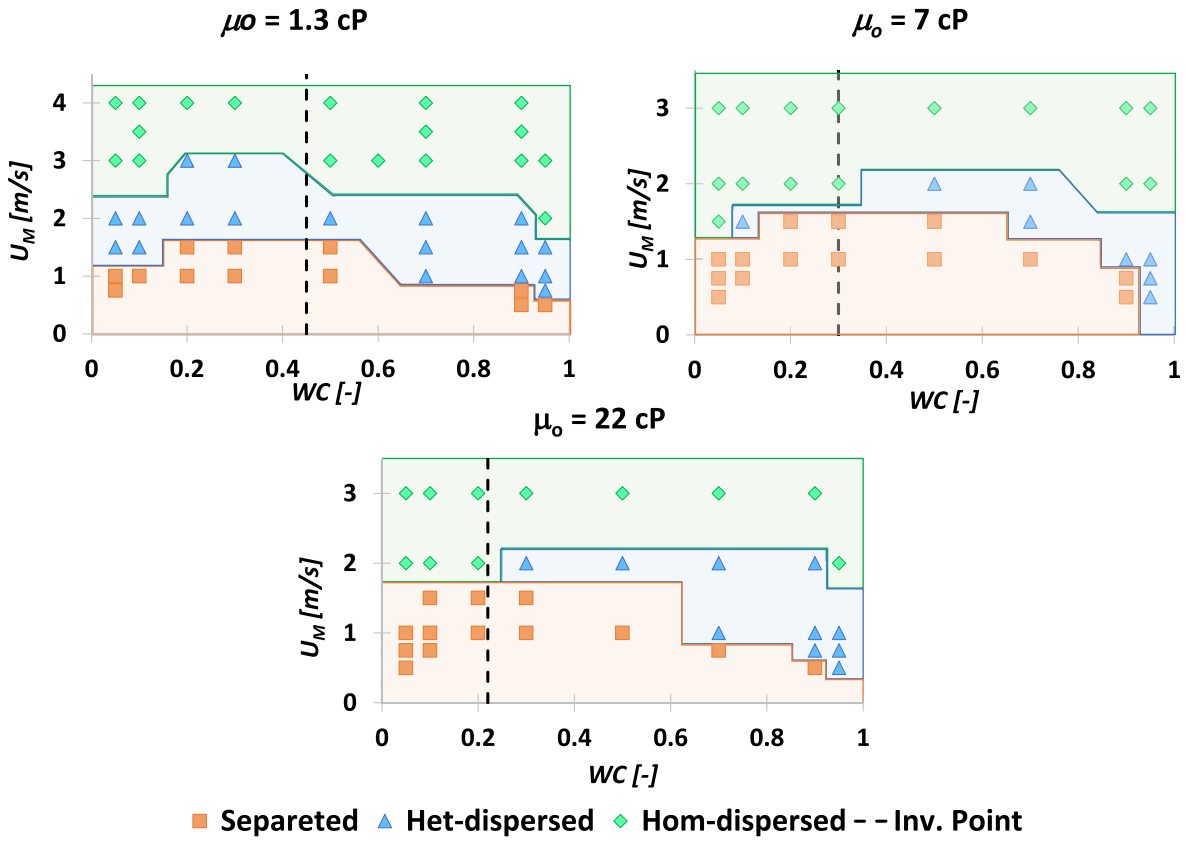


**Fig. 7.** Flow regime maps for each fluid system. The color orange with square symbols represents separated flow, blue with triangles heterogeneous dispersed flow, and green with diamonds homogeneous dispersed flow. The phase inversion WC is indicated by a broken line. (For interpretation of the references to color in this figure legend, the reader is referred to the Web version of this article.)

approximately 0.45, 0.3 and 0.2 respectively, see Fig. 14. Measurements showed good agreement with the inversion point model, equation (7) (Zang and Sarica, 2006)).

$$WC_{inversion} = \frac{1}{1+\tilde{\mu}^{0.4}} \quad with\ \tilde{\mu} = \frac{\mu_{oil}}{\mu_{water}} \tag{7}$$

While the drag reduction phenomena can still be observed for high WCs (water continuous flow) at elevated viscosities, it is less clear for low WCs (oil continuous flow). For better comparison, the pressure drops for all three oils are plotted in the same figures for 1 m/s, 2 m/s and 3 m/s respectively in Fig. 15. Here, we can observe that the pressure drop increases with increasing oil viscosity. However, this is not the case for high WC and $U_M$ when the flow is homogeneously dispersed and water continuous. Here the properties of water, the continuous phase, govern the pressure drop. Also, at 1 m/s and WC = 70%, the pressure drop of oil C shows a peak. While the flow was separated at this point for oil A and B, in case of oil C a heterogeneous dispersion with a dense dispersion layer in the upper part of the pipe was found. This can be observed by comparing Figs. 8–10.

### 5.3. Drag reduction

Fig. 16 shows the relative friction factor as a function of the WC for the three oils tested and mixture velocities of 3 m/s and higher. It was assumed that the same dispersion viscosity model as described in section 3.2 applies for all oils, eq. (5). Based on that, the theoretical friction factor was calculated as $f_0$. The relative friction factor is thus defined as the measured friction factor $f$ divided by $f_0$. From the results we can observe that a noticeable drag reduction is present in the flow loop experiments as well, because the relative friction factor is less than unity. The dashed yellow line presents the predicted relative friction factor based on the drag reduction characterized in section 3.2 and expressed as eq. (6). A very good agreement was found for oil A for both water continuous and oil continuous experiments. Only in the phase inversion region (The phase inversion WC is shown by the vertical dashed lines.), a discrepancy from the prediction was found. The relative friction factor reaches a valley where the drag reduction is stronger than in the mini-loop experiments. Here, effects might occur which are not fully covered by the simple viscosity and drag reduction model. The scatter observed near the phase inversion point, might be explained by the occurrence of a different type of dispersion (dual-continuous dispersion or complex multiple dispersions where droplets are dispersed inside other droplets) or a sudden transition to laminar flow in this region.

Comparing the different oils, we found that the drag reduction is affected by the oil viscosity in oil continuous flow. For the higher oil viscosities, oil B and C, the relative friction factor deviates somewhat for oil continuous flow. First the friction factor increases compared to single-phase oil and later decreases as the water fraction increases. In general, measurements show slightly higher relative friction factors when compared with oil A and the simple model. For oil B and C, it is not clear if the deviation is due to a different dispersion viscosity behavior or drag reduction. Rheology measurements of oil B and C could not be performed in the mini-loop due to limitations set by the pump which was not able to circulate these higher viscosity oils at a sufficiently high rate. On the contrary, the drag reduction in the water continuous flow does not show a dependency on the oil viscosity. Note that the same viscosity model as for oil A was used for oil B and C.

The water fraction required to invert the dispersion is dependent on the oil viscosity. A tendency is observed where the water fraction at the inversion point decreases as the oil viscosity increases. This agrees with observations reported by (Brauner, 2003).

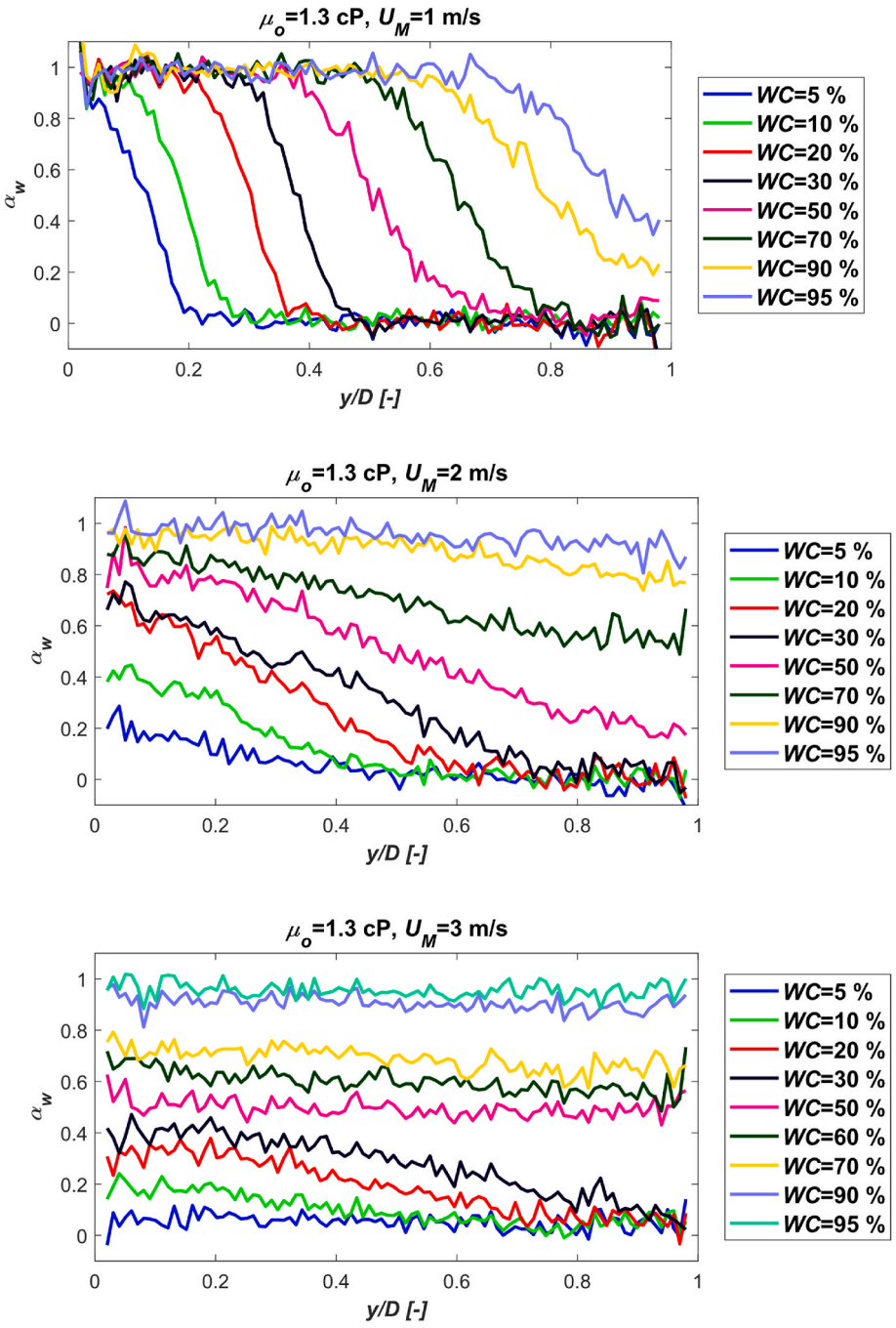


**Fig. 8.** Local water fraction measurement for oil A (1.3 cP) at $U_M$ = 1, 2 and 3 m/s. The input water fractions are shown in the legend.

### 5.4. Droplet size measurements

Droplet measurements were done with help of a particle-sizing camera (CANTY InFlow™). Small sampling tubes were inserted in the test section at three positions along the pipe. The sampling tubes were pointing opposite to the flow direction and could be traversed in the vertical direction, such that samples at different heights could be taken (0.14 cm from bottom, center, 0.86 cm from top). The sampling tubes were connected to the particle-sizer taking in-situ videos of the passing droplets. The droplets were measured and counted using a machine learning algorithm for object detection based on an open-source code in TensorFlow (2020). The algorithm was developed using one of the pre-trained object detection models of TensorFlow, which was re-trained to detect droplets.

The droplet counting obtained with the algorithm was verified by comparison with manual counting done with the program ImageJ. Three random experimental points were selected for the automatic counting verification. Based on previous experiences, at least 1000 droplets were manually counted for each video. Characteristic droplet diameters were estimated for the automatic and the manual counting, for the same test points, and compared against each other. The results are presented in Table 3. The Sauter mean diameter (d32) and dv95 obtained with the automatic counting, deviated from the manual counting by less 7%, for all the experimental points tested. A deviation of less than 10% was considered acceptable, therefore the results from the automatic counting were used to perform a droplet size distribution analysis.

The Sauter mean diameter is the ratio of the droplet volume to its surface area and is defined by equation (8), where $n_i$ and $d_i$ represent the

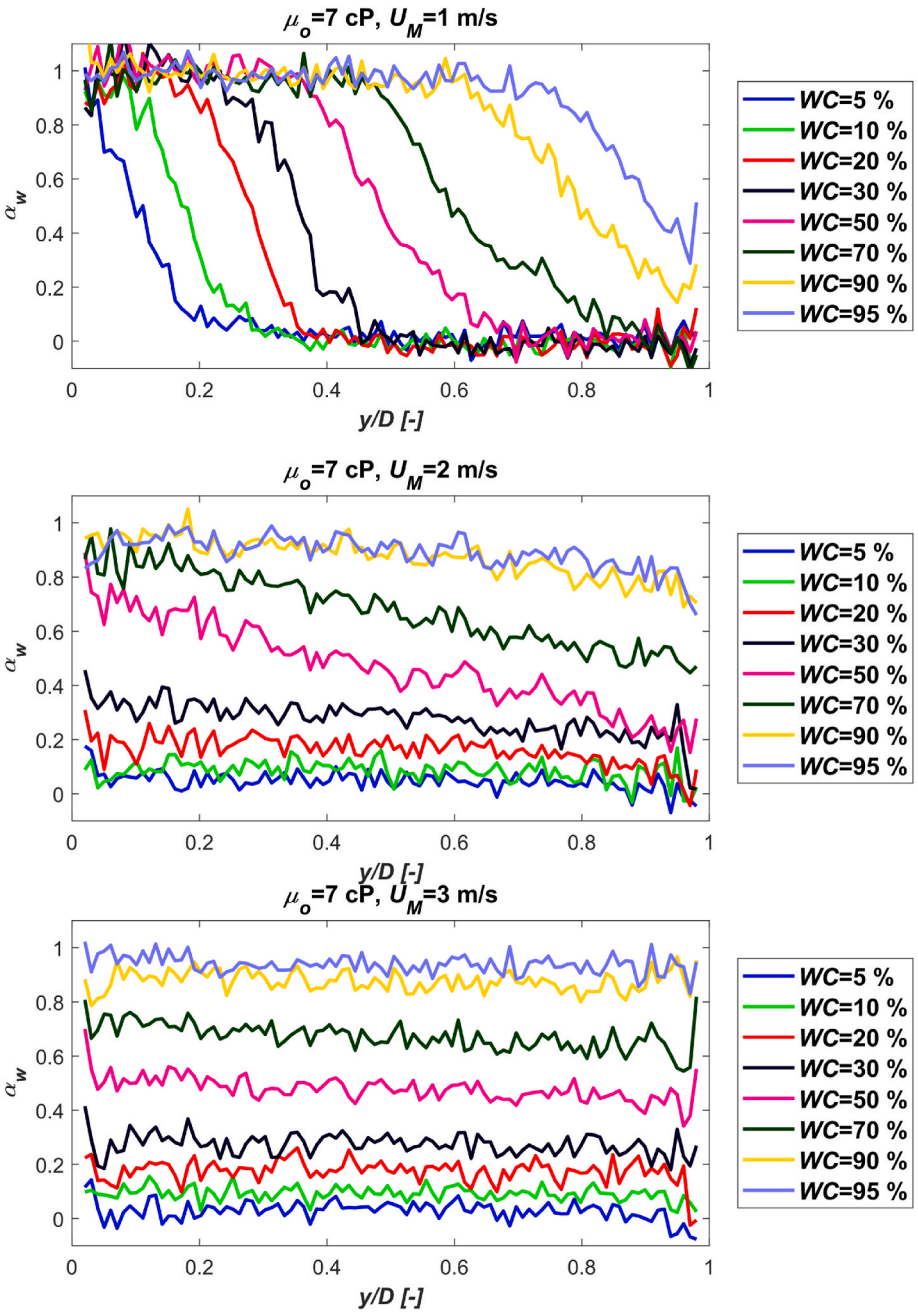


**Fig. 9.** Local water fraction measurement for oil B (7 cP) at $U_M = 1$, 2 and 3 m/s. The input water fractions are shown in the legend.

number and diameter of droplet, respectively. The term dv95 is the droplet size below which the 95% of all the droplets volume is contained.

$$d32 = \sum n_i d_i^3 \Big/ \sum n_i d_i^2 \tag{8}$$

In addition to the counting verification, all the videos were manually inspected and experimental points with bad video quality discarded. An example of the automatic detections is shown in Fig. 17. Different colors present different probabilities for a correct object detection as indicated by the algorithm itself (Blue: P $\geq$ 80%, Red: 60% $\leq$ P $<$ 80%, Green: 40% $\leq$ P $<$ 60%, Yellow: P $<$ 40%; where P: probability).

Figs. 18–20 show the cumulative distribution function obtained for the different oil viscosities, mixture velocities and water cuts of 20% (oil continuous) and 70% (water continuous).

For oil A, when the flow is water continuous (70% WC), the droplet size decreases as the $U_M$ increases, since higher velocity means higher turbulence, which induce to droplet breakup. This tendency is less clear for the oil continuous flow. Some droplet size stratification is observed for water continuous flow at 2 m/s, where the bigger droplets distribute at the top. For oil continuous flow (20% WC) the opposite is the case, with larger droplets at the bottom. This is in agreement with the heterogeneous phase distribution as can be observed from Fig. 8. As the velocity increases, the dispersions become more homogeneous and droplet sizes seem to be uniformly distributed along the vertical position in the pipe's cross section.

The droplet size distributions for oil B and oil C presents a similar behavior as for oil A: The droplet size decreases as $U_M$ increases. However, some differences should be pointed out:

For oil B, the picture quality was not as good as for oil A and C and droplet analysis was challenging. We consider results to be more uncertain as for the other oils. For $U_M = 3$ m/s and 20% WC the processing

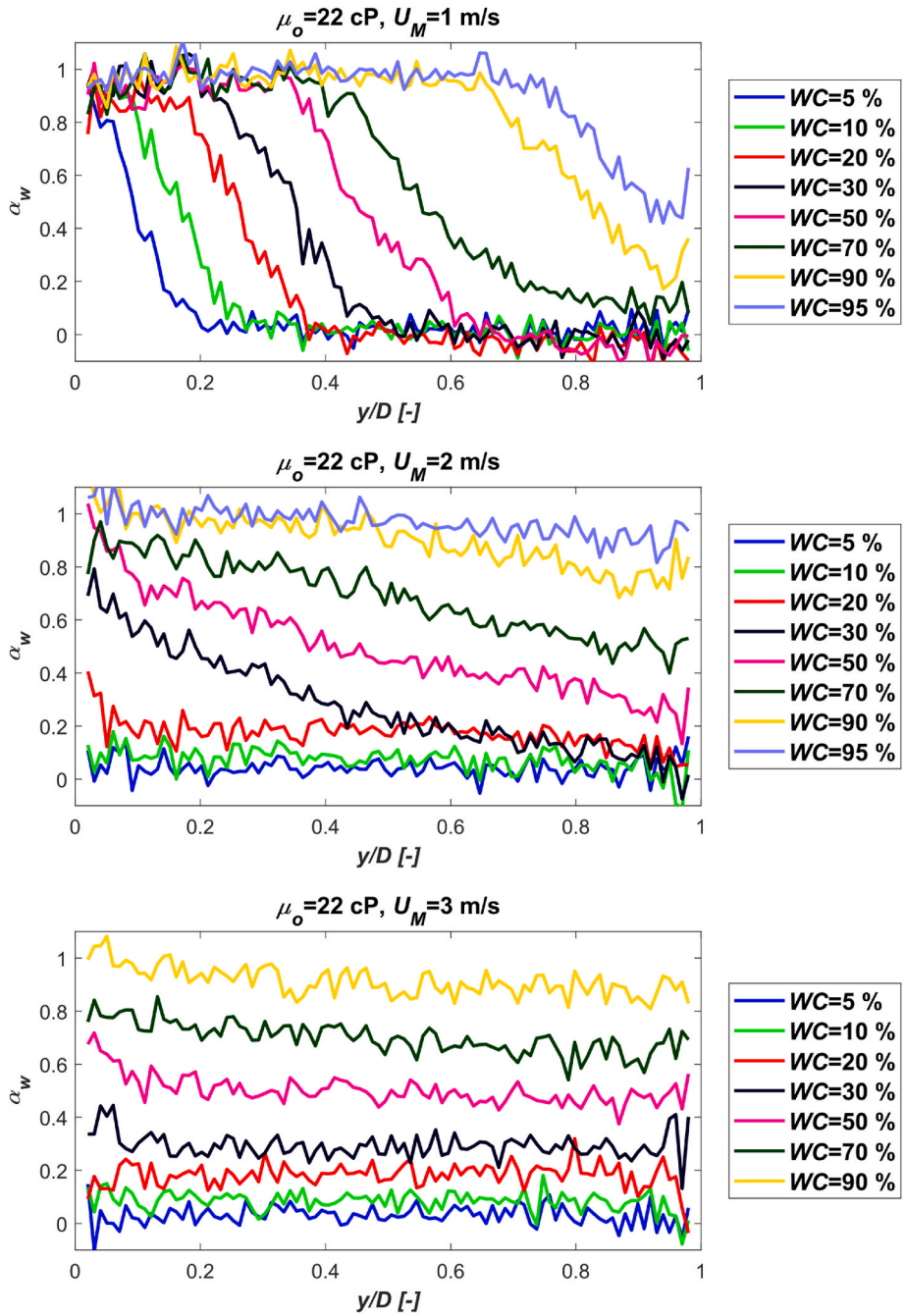


**Fig. 10.** Local water fraction measurement for oil C (22 cP) at $U_M = 1$, 2 and 3 m/s. The input water fractions are shown in the legend.

was not possible. At $U_M = 2$ m/s, and water continuous flow (70% WC), a very distinct droplet size stratification is observed with the bigger oil droplets concentrating at the top of the pipe. For $U_M = 3$ m/s and water continuous flow, the droplet size distributes more homogeneously.

For oil C, stratification is observed at $U_M = 3$ m/s and water fraction 20%. In this case, bigger water droplets were measured at the top of the pipe. This is contrary of what is expected, since the water has higher density than the oil, the bigger droplets should be concentrated at the bottom of the pipe. A possible reason for this could be that the flow is close to its inversion region at this point, and the behavior is more complex and unpredictable. Indeed, in this region, the flow might switch between being oil- and water continuous, and it is thus possible that the associated size distributions contain both oil- and water droplets. A similar behavior was found for oil A at 35% WC and 3 m/s which is close to the inversion point as well for this oil. The stratification observed in the CDF plots, can be verified with the local water fraction, which is presented in Tables 4–6.

Fig. 21 presents examples of the dispersions obtained for each fluid systems. The three images at the top show the droplets when the flow was oil continuous, while the three pictures at the bottom are water continuous flow. These pictures show qualitatively the influences of the oil viscosity on the water-oil dispersion behavior. The droplet size changes notably when the flow is oil continuous. On the other hand, droplets look very similar for water continuous flow.

Fig. 22 shows the cross-sectional average of the Sauter mean diameter against the water fraction for the three oils studied. The plot further compares the measurements (symbols) with the estimated diameter using the Brauner H model for dense dispersions as expressed in eq (9) to eq (11) ((Brauner, 2003). Here, $\rho_c$ is the density of the continuous phase, $\sigma$ the interfacial tension, $We_c$ the critical Weber number of the

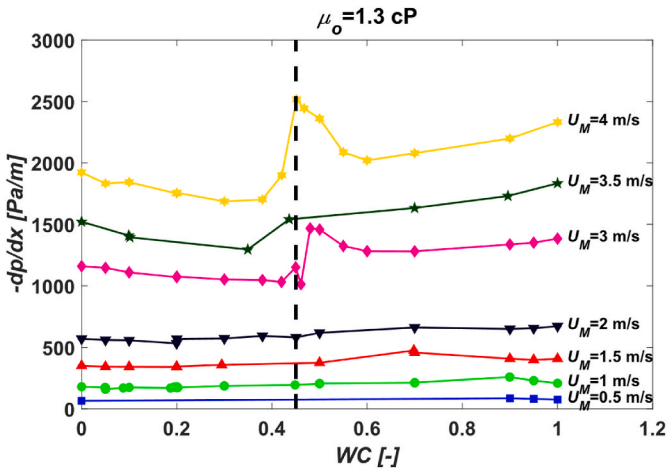


**Fig. 11.** Pressure gradient for oil A (1.3 cP) and different fluid velocities. The dashed vertical line indicates the inversion point.

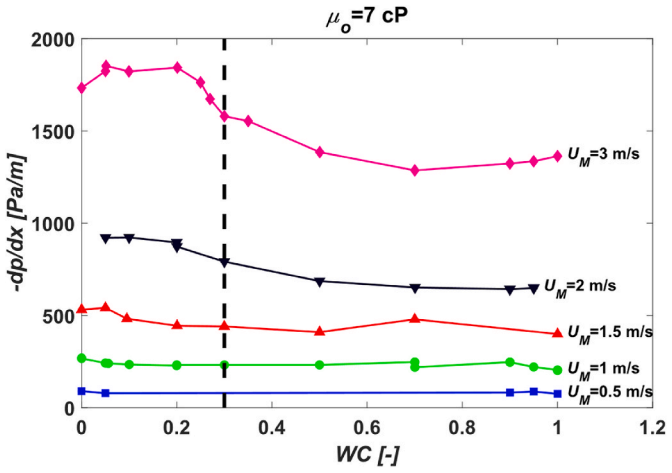


**Fig. 12.** Pressure gradient for oil B (7 cP) and different fluid velocities. The dashed vertical line indicates the inversion point.

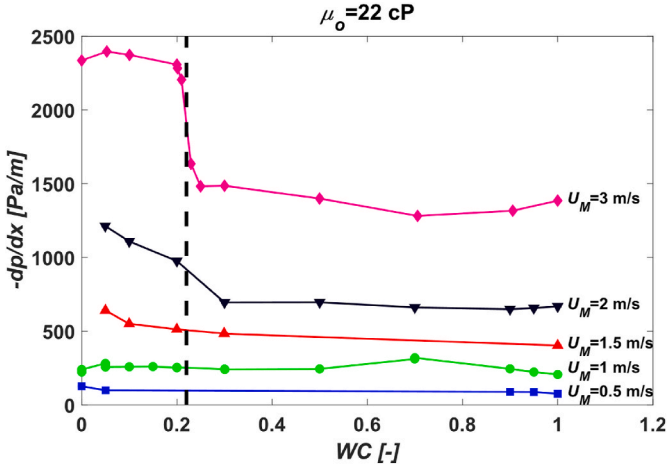


**Fig. 13.** Pressure gradient for oil C (22 cP) and different fluid velocities. The dashed vertical line indicates the inversion point.

continuous phase and $\widetilde{C}_H$ and $k$ are tunable constants. $D$, $\rho$, $\varphi$, and $U$ are, as before, the inner pipe diameter, mixture density, dispersed phase fraction and mixture velocity. The constants used to estimate the droplet

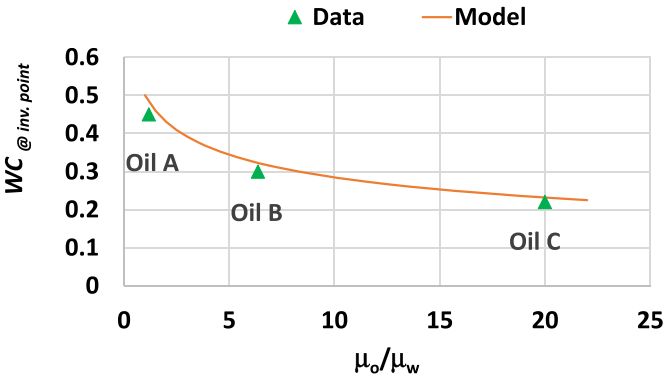


**Fig. 14.** WC at the inversion point for each fluid system.

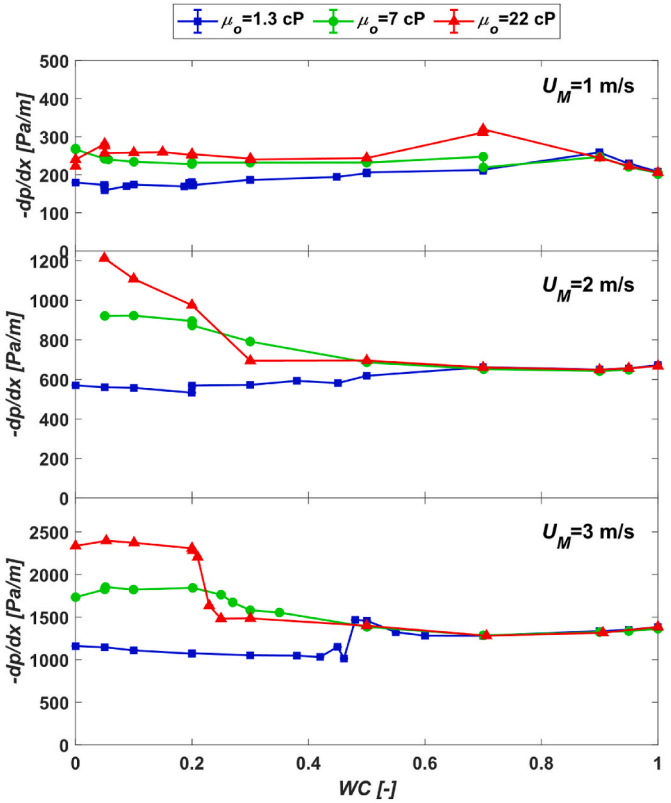


**Fig. 15.** Comparison of pressure drop obtained with each fluid system for different mixture velocities ($U_M$ = 1, 2 and 3 m/s).

diameter are presented in Table 4. Note that the measured friction factor $f$ was used in equation (9). The Brauner H model is an extension of the Hinze model for dense dispersions where droplet-droplet coalescence becomes important. This is expected to be the case in the presented experiments since no stabilizing agents were added and droplets in contact tend to coalesce fast.

From Fig. 22 we observe that the different oils have a marginal influence on the droplet diameter when the flow is water continuous. This was expected as it is mainly the continuous phase properties governing the turbulent shear forces leading to droplet break-up. The slightly different interfacial tension and different dispersed phase (oil) viscosity will have a secondary effect which could explain the minor difference in size. Here oil A gives the smallest droplet sizes. With the lowest IFT and viscosity it provides the weakest resistance to droplet deformation and finally break-up. Opposite droplets are slightly larger for oil C, with the highest IFT and viscosity. In contrast, for oil continuous flow, the type of

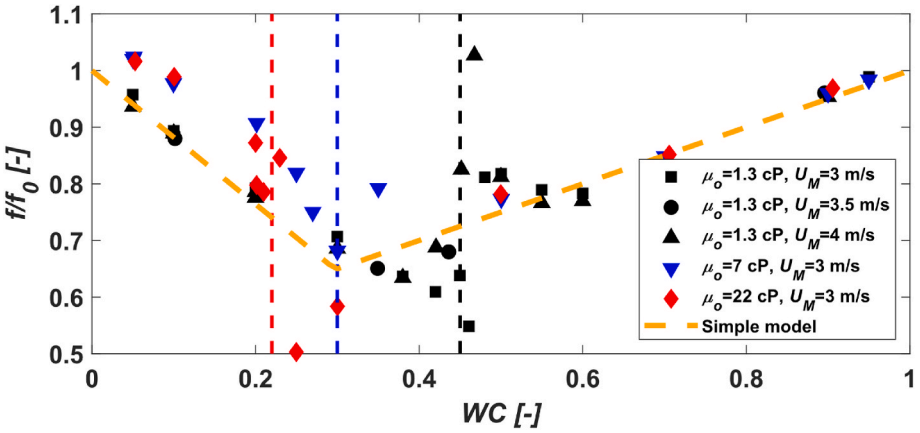


**Fig. 16.** Drag reduction. The plot represents the relative friction factor as function of WC for the three oil viscosities, which is compared against the predicted relative friction factor expressed as eq. (6). The vertical dashed lines represent the inversion point for each fluid system.

**Table 3**
Comparison of droplet sizes obtained with automatic and manual counting.

| | Test point 1 | | | Test point 2 | | | Test point 3 | | |
|---|---|---|---|---|---|---|---|---|---|
| | manual [μm] | automatic [μm] | deviation [%] | manual [μm] | automatic [μm] | deviation [%] | manual [μm] | automatic [μm] | deviation [%] |
| d32 | 321.3 | 303.3 | 5.63 | 863.7 | 822.3 | 4.80 | 390.5 | 388.6 | 0.49 |
| dv95 | 852.5 | 859.9 | 0.86 | 1755.7 | 1728.1 | 1.57 | 1065.7 | 991.6 | 6.95 |

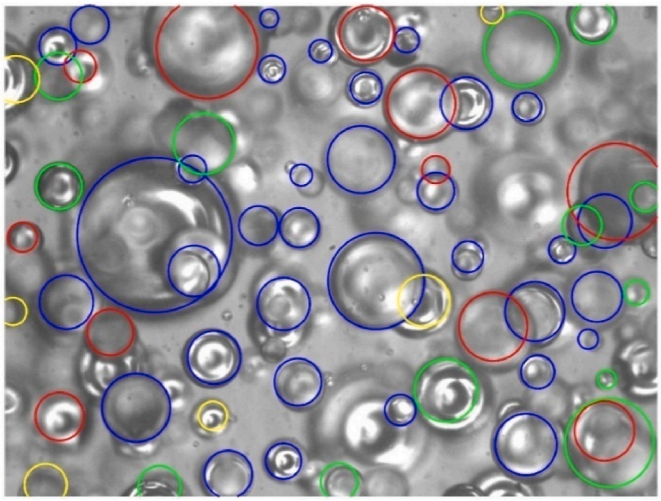

**Fig. 17.** Visual inspection of automatic droplet counting.

oil has a clear effect on the droplet size. The Sauter mean diameter is considerably smaller for the largest oil viscosities. As the oil viscosity increases the viscous shear stress will increase as well and promote droplet breakup. Therefore, the higher the viscosity of the continuous phase (the viscosity of the disperse phase remains constant) the smaller the droplet diameters.

With the H model by Brauner the measured droplet sizes could be reproduced relatively well for water-continuous points and qualitatively well for oil-continuous points. In the inversion region the deviation was larger. However, as summarized in Table 7, different constants had to be used for the variable $\widetilde{C}_H$, meaning that the variable is sensitive to the fluids used and type of dispersion. Thus, the model is not fully predictive. $\widetilde{C}_H$ was relatively similar for oil A and C, but much smaller for oil B. This was surprising because oil B is a mixture of oil A and C. As mentioned before, the quality of the measurements for oil B was not as good as for oil A and C. However, we are not sure if this uncertainty can explain such a large deviation.

$$(\widetilde{d}_{max})_\varepsilon = \left(\frac{d_{max}}{D}\right)_\varepsilon = 2.22\widetilde{C}_H We_c^{-0.6}\left(\frac{\varphi}{1-\varphi}\right)^{0.6}\left[\frac{\rho}{\rho_c(1-\varphi)}f\right]^{-0.4} \quad (9)$$

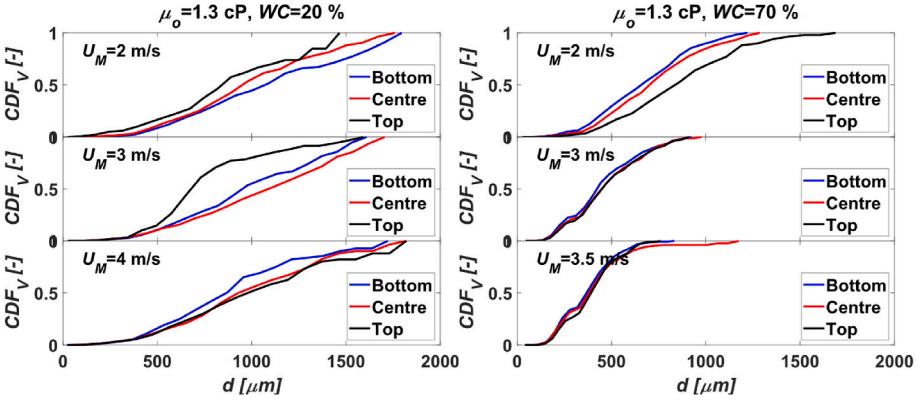


**Fig. 18.** CDF of droplet size for oil A (1.3 cP) at several $U_M$.

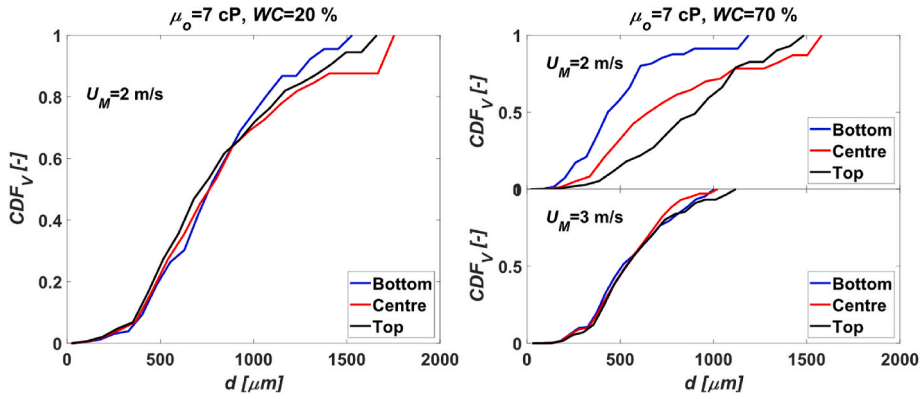


**Fig. 19.** CDF of droplet size for oil B (7 cP) at several $U_M$.

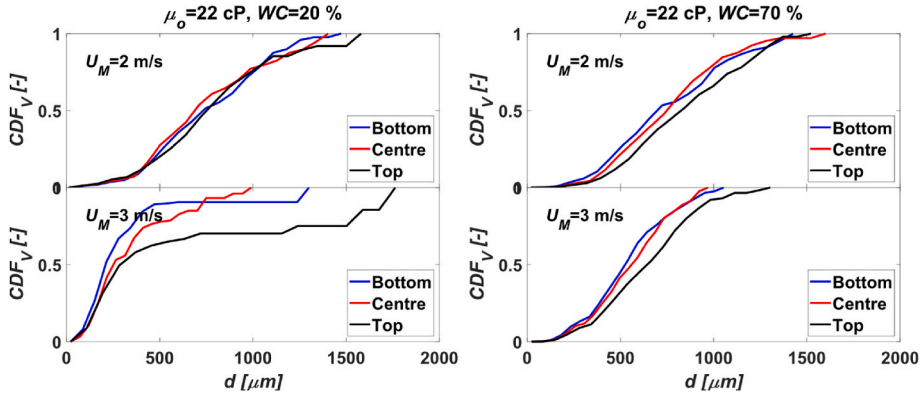


**Fig. 20.** CDF of droplet size for oil C (22 cP) at several $U_M$.

**Table 4**
Local water fraction for oil A and the conditions presented in Fig. 18.

| | | Local water fraction ($\alpha_W$) | | | |
|---|---|---|---|---|---|
| | | $U_M = 2$ m/s | $U_M = 3$ m/s | $U_M = 3.5$ m/s | $U_M = 4$ m/s |
| 1.3 cP WC = 20% | Top | 0.05 | 0.07 | – | 0.13 |
| | Center | 0.12 | 0.19 | – | 0.18 |
| | Bottom | 0.58 | 0.32 | – | 0.24 |
| 1.3 cP WC = 70% | Top | 0.55 | 0.65 | 0.66 | – |
| | Center | 0.71 | 0.69 | 0.66 | – |
| | Bottom | 0.85 | 0.71 | 0.71 | – |

**Table 5**
Local water fraction for oil B and the conditions presented in Fig. 19.

| | | Local water fraction ($\alpha_W$) | |
|---|---|---|---|
| | | $U_M = 2$ m/s | $U_M = 3$ m/s |
| 7 cP WC = 20% | Top | 0.11 | – |
| | Center | 0.18 | – |
| | Bottom | 0.20 | – |
| 7 cP WC = 70% | Top | 0.52 | 0.63 |
| | Center | 0.68 | 0.68 |
| | Bottom | 0.86 | 0.72 |

**Table 6**
Local water fraction for oil C and the conditions presented in Fig. 20.

| | | Local water fraction ($\alpha_W$) | |
|---|---|---|---|
| | | $U_M = 2$ m/s | $U_M = 3$ m/s |
| 22 cP WC = 20% | Top | 0.14 | 0.19 |
| | Center | 0.16 | 0.16 |
| | Bottom | 0.17 | 0.17 |
| 22 cP WC = 70% | Top | 0.49 | 0.64 |
| | Center | 0.70 | 0.67 |
| | Bottom | 0.87 | 0.76 |

$$We_c = \frac{\rho_c U^2 D}{\sigma} \tag{10}$$

$$1.5 \leq \frac{dmax}{d32} = k \leq 3 \tag{11}$$

## 6. Conclusions

Oil-water pipe flow experiments were conducted for three different oil viscosities, and local water fraction profiles, pressure drop, and droplet sizes analyzed.

Three main flow regimes were identified, namely separated flow, heterogeneously dispersed flow, and homogeneously dispersed flow. The occurrence of a specific flow regime and the transition from between them are greatly influenced by the mixture velocity and the water cut WC. Specifically, the transition takes place at lower $U_M$ for low and high WC. With increasing oil viscosity, the transition region was found to become smaller for low water cuts and the flow almost immediately turns into a homogenous oil-continuous dispersion.

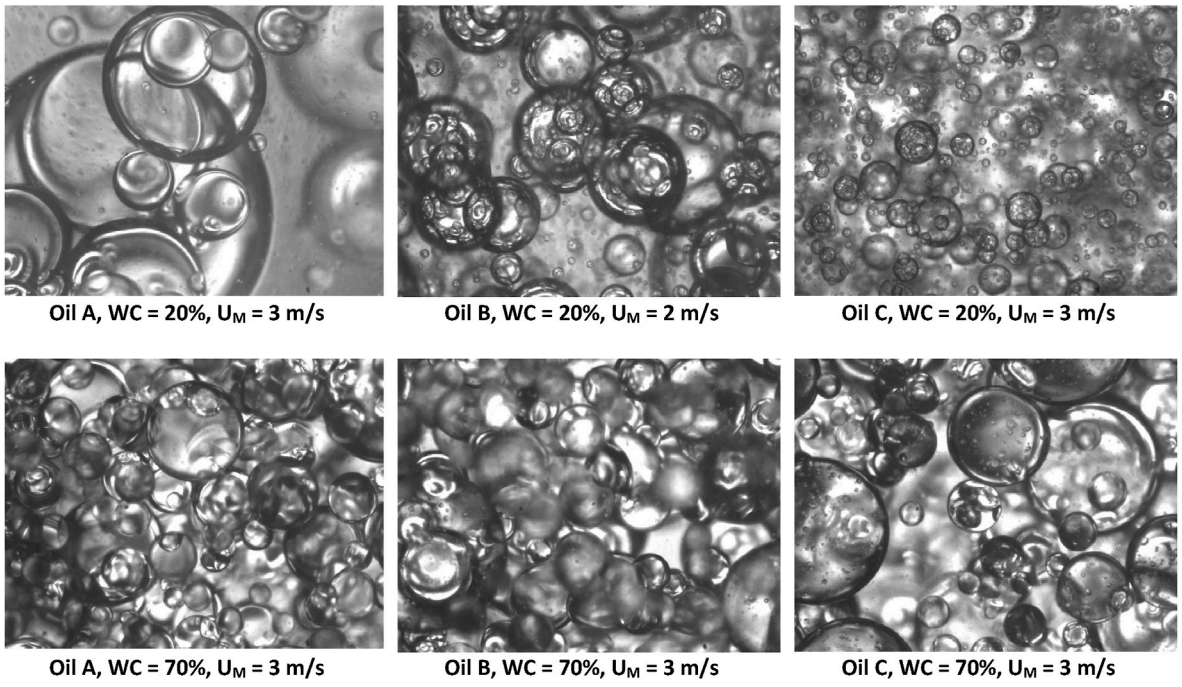


**Fig. 21.** Example of droplet pictures obtained for the different fluid systems studied and continuity.

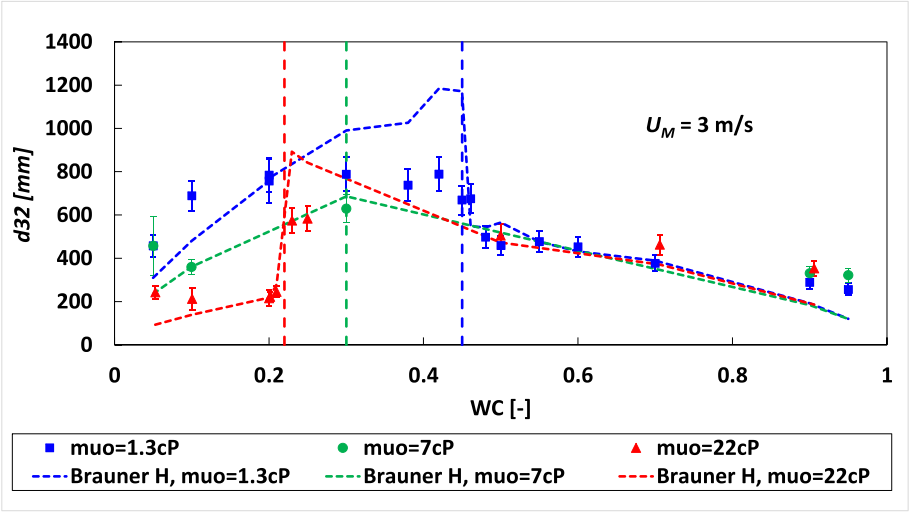


**Fig. 22.** Sauter mean diameter. Comparison between $d_{32}$ from the droplet images data and Brauner model for each fluid system.

**Table 7**
Constants used to estimate the Sauter mean diameter using Brauner H model for dense dispersions.

| | $\widetilde{C}_H$ (oil continuous) | $\widetilde{C}_H$ (water continuous) | $k$ | WC @ inversion point |
|---|---|---|---|---|
| Oil A | 0.646 | 0.226 | 1.551 | 0.450 |
| Oil B | 0.216 | 0.226 | 1.551 | 0.300 |
| Oil C | 0.550 | 0.226 | 1.551 | 0.220 |

The oil viscosity also influences the pressure gradient when the flow is oil continuous. Higher pressure gradient is observed for higher oil viscosity because the wall shear stress increases with increasing viscosity. For the higher velocities, when the flow was fully dispersed, a peak was observed for the oil A when the water fraction reaches the inversion point. For oil B and oil C, no peak was observed, but the inversion point could clearly be identified by an abrupt decrease in the pressure drop. The oil viscosity also affects the inversion point of the dispersion, as the viscosity increases, the inversion point occurs at lower WCs. Measurements were in good agreement with a theoretical model.

Significant drag reduction has been observed for dispersed flow of both oil- and water-continuous dispersions. Special characterization experiments for oil A were performed in a pipe rheometer where the effects of dispersion viscosity and drag reduction were isolated. and the results were expressed in a simple model. Very good agreement was achieved when the model was used to predict the pressure drop for oil A in the pipe flow experiments in the medium scale flow loop. For oils B and C, we found that the drag reduction effect was slightly smaller than for oil A. However, for oils B and C we did not conduct pipe rheometer experiments, so the drag reduction calculation was based on using the same dispersion viscosity model as found for oil A. Consequently, we

cannot rule out that the differences may have been due to differences in the dispersion viscosity.

Finally, the influence of the oil viscosity on the droplet size is very significant for oil continuous flow. Here, the higher the viscosity, the smaller the droplet size as consequence of the higher shear stress. On the other hand, the oil viscosity only has a minor effect on the oil droplet sizes in water continuous flows. The velocity also influences the droplet size. More stratification of the droplets is observed for the lower velocities. Also, for the water continuous flow, the droplet size tends to decrease as $U_M$ is increased, since higher turbulence induces increased breakup. The droplet size model by Brauner (2003) was compared to the measured Sauter mean droplet sizes, and a good qualitative agreement could be obtained by tuning the model coefficients for each of the fluids.

A limitation of the experimental work was the quality of the droplet images for some test points, leading to a higher uncertainty in the droplet data. Improved sampling equipment might be used in the future. Furthermore, pipe rheometer measurements for oil B and C could not be conducted due to limitations of the pump. The presented data is also limited to unstable fluid systems. Further experiments with stabilized model oils or real crude oils are planned as future work in order to investigate fluid chemistry effects.

## Author statement

**Diana Gonzalez**: Formal analysis, Writing – original draft, Visualization, Writing – review & editing. **Heiner Schümann**: Conceptualization, Methodology, Investigation, Writing – review & editing, Supervision, Project administration, Funding acquisition. **Jørn Kjølaas**: Conceptualization, Methodology, Formal analysis, Data curation, Writing – review & editing, Supervision.

## Declaration of competing interest

The authors declare that they have no known competing financial interests or personal relationships that could have appeared to influence the work reported in this paper.

## Data availability

The data was shared on Mendeley Data Repository.

## Acknowledgements

The work is part of Nexflow, a knowledge-building project for industry (NFRproject number 295035) and would not have been possible without the financial support by TotalEnergies EP Norge AS and the Research Council of Norway. We further acknowledge Bendik Sægrov for analyzing the large number of droplet pictures taken during the experiments.

## Appendix A. Supplementary data

Supplementary data to this article can be found online at https://doi.org/10.1016/j.petrol.2022.110996.

## References

Angeli, P., 1996. Liquid-liquid dispersed flows in horizontal pipes. In: Department of Chemical Engineering and Chemical Technology. Imperial College of Science, Technology and Medicine, London.

Angeli, P., Hewitt, G., 1998. Pressure gradient in horizontal liquid-liquid flows. Int. J. Multiphas. Flow 24, 1183–1203.

Barton, C., Albaugh, E., Davis, D., 2019. 2019 Deepwater Technologies & Solutions for Concept Selection [Internet] Available at: https://www.offshore-mag.com/resources/maps-posters/document/14036485/wood-2019-deepwater-technologies-solutions-for-concept-selection.

Brauner, N., 2003. Liquid-liquid two-phase flow systems. In: Modelling and Experimentation in Two-phase Flow. Springer, Vienna.

Elseth, G., 2001. An experimental study of oil/water flow in horizontal pipes. In: Department of Technology (HiTTF). Telemark University College, Porsgrunn.

Karabelas, A.J., 1978. Droplet size spectra generated in turbulent pipe flow of dilute liquid/liquid dispersions. AIChE J. 24 (2).

Kjølaas, J., Wolden, M., 2021. Onset of water accumulation in oil/water pipe flow – experiments and modelling with LedaFlow. Int. J. Multiphas. Flow Volume 134. (2021) 103469. https://doi.org/10.1016/j.ijmultiphaseflow.2020.103469.

Kumara, W., Halvorsen, B., Melaaen, M., 2009. Pressure drop, flow pattern and local water volume fraction measurements of oil-water flow in pipes. Meas. Sci. Technol. 20 (11).

Nädler, M., Mewes, D., 1997. Flow induced emulsification in the flow of two immiscible liquids in horizontal pipes. Int. J. Multiphas. Flow 23 (1).

Ngan, K.H., 2011. Phase inversion in dispersed liquid-liquid pipe flow. In: Department of Chemical Engineering. Unviversity College London, London.

OG21 group, 2021. OG21 - A New Chapter: Oil and Gas for the 21st Century. The Research Council of Norway.

Omer, A., Pal, R., 2013. Effects of surfactant and water concentrations on pipeline flow of. Ind. Eng. Chem. Res. 52 (26), 9099–9105.

Pal, R., 1993. Pipeline flow of unstable and surfactant-stabilized emulsions. AIChE J.

Pal, R., 1996. Effect of droplet size on rheology of emulsions. AIChE J. 42 (11), 3181–3190.

Pal, R., 2007. Mechanism of turbulent drag reduction in emulsions and bubbly suspensions. *Ind. Eng. Chem. Res.,* Volum 46, 618–622.

Pal, R., Rhodes, E., 1989. Viscosity/concentration relationships for emulsions. J. Rheol. 33.

Picchi, D., et al., 2015. An experimental investigation and two-fluid model validation for dilute viscous oil in water dispersed pipe flow. Exp. Therm. Fluid Sci. 60, 28–34.

Pinho, F., Li, C., Younis, B., Sureshkumar, R., 2008. A low Reynolds number turbulence closure for viscoelastic fluids. J. Non-Newtonian Fluid Mech. 154 (2–3), 89–108.

Rodriguez, O., Oliemans, R., 2006. Experimental study on oil–water flow in horizontal and slightly inclined pipes. Int. J. Multiphas. Flow 32 (3), 323–343.

Rodriguez, I., et al., 2012. Drag reduction phenomenon in viscous oil-water dispersed pipe flow: experimental investigation and phenomenological modeling. AIChE Journal, Transport Phenomena and Fluid Mechanics 58 (9), 2900–2910.

Soleimani, A., 1999. Phase Distribution and Associated Phenomena in Oil-Water Flows in Horizontal Tubes. Imperical College Lodon, London.

Strømsheim, G., Haugnes, G., 2012. Rørene Gjorde Oljeeventyret Mulig [Transl: "The Pipes that Made the Oil Adventure Possible"]. Aftenposten.

TensorFlow, 2020. TensorFlow 2 Object Detection API Tutorial [Internet] Available at: https://tensorflow-object-detection-api-tutorial.readthedocs.io/en/latest/ [Found 2021].

Valle, A., 1998. Multiphase pipeline flows in hydrocarbon recovery. Multiphas. Sci. Technol. 10 (1), 1–139.

Valle, A., 2000. Three Phase Gas-Oil-Water Pipe Flow. Department of Chemical Engineering and Chemical Technology, Imparial College of Science, Technology and Medicine, London.

Zang, H.-Q., Sarica, C., 2006. Unified Modeling of Gas/Oil/Water-Pipe Flow - Basic Approaches and Preliminary Validation. Dallas, June 2006. SPE Projects, Facilities & Construction.